A molecular picture of motion in polyolefins

Erin K. Boland,[1] Jiahong Liu,[1] and Janna K. Maranas[2,a)]
[1]*Department of Chemical Engineering, The Pennsylvania State University, University Park, Pennsylvania 16802, USA*
[2]*Departments of Chemical Engineering and Material Science, The Pennsylvania State University, University Park, Pennsylvania 16802, USA*

(Received 9 December 2009; accepted 25 February 2010; published online 13 April 2010)

We examined three united atom models in light of their description of polyolefin dynamics and investigated the relative influence of various potentials on the resulting dynamics. Results were compared with a collection of experimental data on polyethylene, poly(ethylene-*alt*-propylene), polypropylene, and head-to-head polypropylene, including quasielastic neutron scattering measurements that we report for two of these materials. For materials with branching, differences between force fields are apparent at low temperature, with the NERD force field most accurate. Differences between NERD and the others are the strength of nonbonded interactions and the height of torsional barriers. We artificially raised each, both of which leads to a slow down in dynamics similar to that observed when lowering temperature. Increasing nonbonded interaction strength slows dynamics with the Vogel dependence of the α-relaxation, while raising torsional barriers, slows dynamics with the Arrhenius dependence of the β-relaxation. © *2010 American Institute of Physics*. [doi:10.1063/1.3366660]

I. INTRODUCTION

Polyolefins, saturated hydrocarbon polymers, are an industrially significant material and represent a multibillion dollar subset of the chemical industry. An understanding of dynamics and the mechanisms from which they arise is important for the processing of these materials. The dynamics of polymer melts span a large range of length and time scales, and many experimental techniques probe these motions including: nuclear magnetic resonance spectroscopy (NMR),[1–3] dielectric spectroscopy,[4–6] light and neutron scattering,[7–11] and rheology.[12,13] Molecular simulation can compliment these methods by facilitating the assignment of the molecular level motions underlying experimental observables.

Polyolefins received considerable attention in the simulation community,[14–26] and several force fields have been developed to model these materials.[22,23,27–33] This contribution examines the descriptions of dynamic processes associated with these force fields. The results highlight what interactions are important in describing dynamics in general, as well as providing guidance to those wishing to choose a force field to model dynamic processes in polyolefins. We focus on atomistic modeling at the united atom (UA) level, which represents a balance between computational efficiency and atomistic detail. At this level, long chain properties such as entanglement and reptation are only barely accessible,[34] and the detailed motions of protons, for example the rotation of methyl groups, are excluded. With UA modeling, unentangled systems may be simulated at temperatures in the melt state above T_g, giving access to the high frequency end of the structural relaxation. The range is accessible experimentally using quasi-elastic neutron scattering, a technique which we use to place our results in context with experimental measurements. We study three available UA force fields: NERD,[30–32] OPLS,[27] and TraPPE.[28,29] The main differences between these force fields are in the description of nonbonded or intermolecular interactions, and torsional barrier heights. Thus we are able to describe the influence of these differences on dynamic processes. We further explore the connection of both interactions to dynamic processes by performing computational "experiments" with artificially large barrier heights and intermolecular interaction strengths.

II. SIMULATION DETAILS

Simulation model. Figure 1 shows the repeat units for the materials we consider: polyethylene (PE), polypropylene (PP), head-to-head polypropylene (hhPP) and poly(ethylene-*alt*-propylene) (PEP), whose chain architectures differ in the presence and frequency of methyl group branches. We simu-

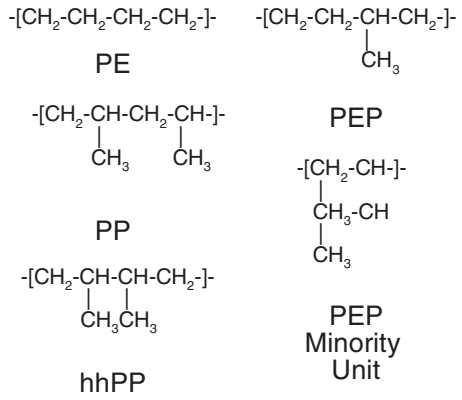

FIG. 1. Repeat units of aPP, hhPP, PE, and PEP. The PEP minority unit appears as 7% of the total number of repeat units.

a)Electronic mail: jmaranas@psu.edu.

TABLE I. Interaction parameters. Potentials which vary significantly between force fields are listed in boldface.

Bond bending: $U_{\text{bend}}=k_b(\theta-\theta_o)^2$

	OPLS		NERD		TraPPE	
Pair identity	k_b (kcal/mol rad^2)	θ_o (deg)	k_b (kcal/mol rad^2)	θ_o (deg)	k_b (kcal/mol rad^2)	θ_o (deg)
$CH_x-CH_x-CH_x$	62.09	114	61.6	114	61.6	114

Bond torsion: $U_{\text{dihedral}}=\Sigma a_i \cos^i \phi$

	Pair identity	OPLS	NERD	TraPPE
a_0 (kcal/mol)	X-CH_2-CH_2-X	2.007	2.006	1.967
	X-CH_2-CH-X	**0.814**	**0.812**	**0.785**
	X-CH-CH-X	**0.292**	**0.900**	**0.785**
a_1 (kcal/mol)	X-CH_2-CH_2-X	4.012	4.012	4.052
	X-CH_2-CH-X	**1.792**	**1.880**	**1.779**
	X-CH-CH-X	**1.128**	**1.128**	**1.779**
a_2 (kcal/mol)	X-CH_2-CH_2-X	0.271	0.271	0.271
	X-CH_2-CH-X	**0.389**	**0.480**	**0.445**
	X-CH-CH-X	**0.670**	**0.373**	**0.445**
a_3 (kcal/mol)	X-CH_2-CH_2-X	−6.290	−6.290	−6.290
	X-CH_2-CH-X	**−3.673**	**−3.550**	**−3.508**
	X-CH-CH-X	**−2.840**	**−4.342**	**−3.508**

Improper torsion: $U_{\text{improper torsion}}=k_{\text{improper torsion}}(\xi-\xi_o)^2$

	$k_{\text{improper torsion}}$ (kcal/mol):	40	ξ_o (deg):	27.25
All force fields:				

Lennard-Jones:

$$U_{L-J}=4\epsilon_{ij}\left[\left(\frac{\sigma_{ij}}{r_{ij}}\right)^{12}-\left(\frac{\sigma_{ij}}{r_{ij}}\right)^{6}\right]$$

$$\epsilon_{ij}=\sqrt{\epsilon_i\epsilon_j},\quad \sigma_{ij}=0.5(\sigma_i+\sigma_j)$$

UA identity	OPLS		NERD		TraPPE	
	σ (Å)	ϵ (kcal/mol)	σ (Å)	ϵ (kcal/mol)	σ (Å)	ϵ (kcal/mol)
CH_3-CH_2	3.905	0.175	3.910	0.165	3.750	0.195
CH_3-CH	**3.910**	**0.160**	**3.850**	**0.139**	**3.750**	**0.195**
CH_2	3.905	0.118	3.930	0.091	3.950	0.091
CH	**3.850**	**0.080**	**3.850**	**0.079**	**4.680**	**0.020**

late atatic PP (aPP) with the exception of comparison to wide angle scattering (WAXS) data for which isotatic PP (iPP) is required. The potential used in all three force fields is a sum of four terms:

$$U = U_{\text{bend}} + U_{\text{dihedral}} + U_{\text{improper torsion}} + U_{\text{Lennard-Jones}}, \quad (1)$$

with covalent bond distances of 1.54 Å maintained using the RATTLE algorithm.[35] We compile the bonded and nonbonded potentials in Table I. When necessary, the torsion potentials have been rewritten so that the *trans*-position occurs at 0° and to reflect the functional form used in this work. Distinctions are made between different types of CH_3 atoms, depending on their local environment: CH_3 united atoms are differentiated as CH_3-X, where X is the identity of the united atom to which it is connected. Thus with respect to the Lennard-Jones potential, the notation CH_3-CH refers to a CH_3 united atom bonded to a CH united atom and not the CH_3-CH interaction, unless otherwise specified. The potentials showing the greatest variation among the force fields are highlighted with bold text: these are torsion about the chain backbone introduced by branching (CH_2-CH and CH–CH bonds) and intermolecular interactions of the branch point CH. Torsional potentials are plotted in Fig. 2, where they have been vertically shifted to 0 kcal/mol at the *trans*-position to facilitate a visual comparison of barrier heights. The Lennard-Jones potentials are compared in Fig. 3 for the branch point CH, the backbone CH_2 group, and the branch CH_3-CH. Methyl groups forming chain ends, CH_3-CH_2, constitute a small fraction of the simulation and are not shown. With the exception of chain ends, CH_2 is the only group in PE. The potentials involving CH_2 vary little among force fields and thus we expect little difference in dynamics. For the branched materials PEP and aPP, the CH and CH_3 groups become important, and rotation occurs about the

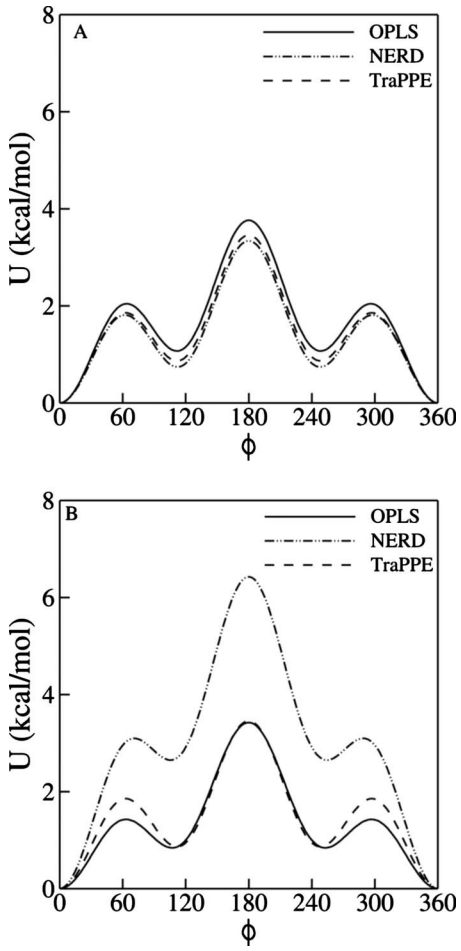

FIG. 2. Comparison of X-CH–CH_2-X (a) and X-CH–CH-X (b) torsional potentials. The torsional angle is defined such that $\phi=0$ indicates a *trans*-sequence. Potentials are shifted vertically such that all force fields have $U(\phi=0)=0$.

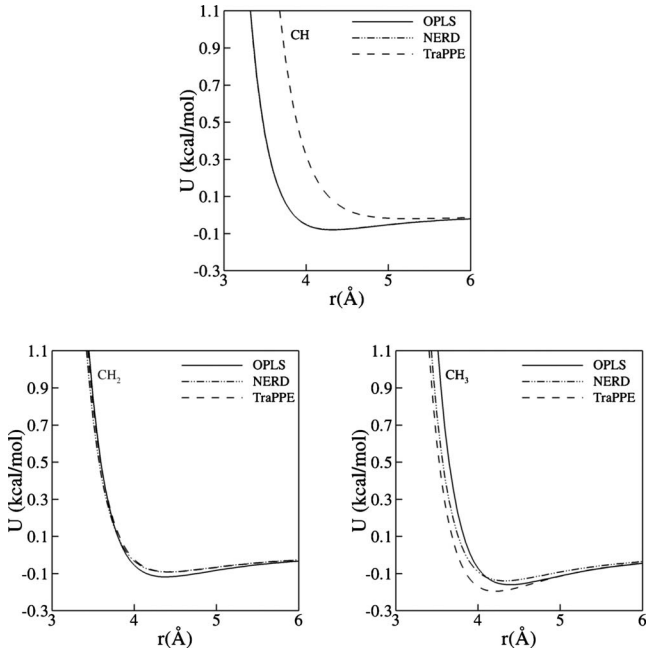

FIG. 3. Comparison of CH, CH_2, and CH_3 Lennard-Jones potentials. The CH_3–CH potential is used for the CH_3 comparison.

CH–CH_2 bond. Barrier heights for rotation about this bond vary by ~7%. Interactions between nonbonded branch [CH_3] groups have moderate differences (interaction strengths vary by about 30%), whereas those of the branch point CH are significantly different in the TraPPE force field. Both torsional rotations and the strength of nonbonded interactions impact polymer dynamics.[36–38] The NERD force field has the lowest barrier for rotation around backbone bonds (X-CH–CH_2-X, where X indicated any united atom), and the weakest CH_3 nonbonded interactions, both of which suggest that it will have faster dynamics than the other two. The TraPPE force field has a significantly softer CH nonbonded potential, which also suggests faster dynamics. Thus for PEP and aPP, the OPLS force field should produce the slowest dynamics, with the ordering of the other two unclear. For hhPP, we must also consider rotation around the CH–CH bond, the most significant variation in any single potential. The OPLS force field has the lowest barrier, with that for the NERD force field significantly higher. Because this suggests faster dynamics for the OPLS model, the effect of this combined with nonbonded interactions and rotation about the CH_2–CH bond is unclear.

The simulations are designed to reflect the molecular weight of the experiment to which they are compared when possible. We consider chains with 40–100 backbone carbon atoms and adopt a nomenclature consisting of the material name and a number indicating the number of backbone carbon atoms. For example, PE100 refers to a simulation ensemble of PE chains, each with 100 backbone atoms. The equations of motion are integrated by the velocity Verlet algorithm[39] using a 5 fs time step. All simulations are performed in the canonical (N,V,T) ensemble. We consider temperatures between an upper limit of 510 K and a lower limit at which the systems become difficult to equilibrate in a reasonable time. The temperature is maintained at the desired value using the Berendsen velocity-rescaling algorithm.[40] The box size V is set based on the number of chains and the density of the material. Because PE oligomer densities are available over a range of molecular weights,[41,42] we scale all material densities based on the oligomer/polymer ratio of PE:

$$\rho_N^i = \rho_{\text{polymer}}^i \left(\frac{\rho_N^{\text{PE}}}{\rho_{\text{polymer}}^{\text{PE}}} \right). \tag{2}$$

Here, N represents the total number of carbon atoms in each chain. We account for the variation of the density with temperature using available experimental measurements of the thermal expansion coefficients, α_i:

$$\frac{1}{\rho(T)} = \frac{1}{\rho(T_{\text{ref}})} \exp[-\alpha_i (T_{\text{ref}} - T)], \tag{3}$$

where the α_i, $\rho(T_{\text{ref}})$, and T_{ref} for all materials are reported in Ref. 43.

To ensure that each chain samples the available configurational space, each simulation is equilibrated for one decay time of the end-to-end vector ACF or 5 ns, whichever is longer. To assess the equilibration criteria, we calculate the intermolecular portion of the radial distribution function g(r)

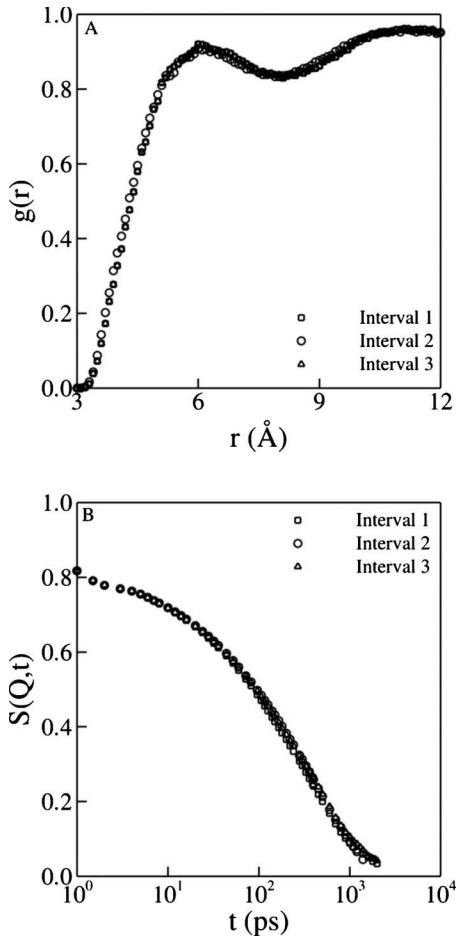

FIG. 4. Assessment of equilibration period. The intermolecular radial distribution function (a) and the self intermediate scattering function at Q =0.99 Å^{-1} (b) are shown for PEP at 294 K over three consecutive 3 ns time intervals.

and the self-intermediate scattering function $S(Q,t)$ of PEP at 294 K over three consecutive 3 ns time intervals after the equilibration period. PEP is chosen as a representative example because it has one of the longest ACF decay times and the lowest simulation temperature. As demonstrated in Fig. 4, no drift is observed in the structural or dynamic properties of PEP after equilibration.

The temperature, molecular weight, density, box size, and the ACF decay time are summarized in Table II for all simulations. The chain dimensions do not vary significantly between simulations performed with different force fields and are reported for the OPLS force field only. We report the longest ACF time for each material at each temperature: those produced by the TraPPE force field for hhPP and those produced by the OPLS force field for all other materials. We set the number of polymer chains to result in box sizes of at least $3R_g$, where R_g is the average radius of gyration of the polymers after equilibration, at the highest density simulated. For polymers with a backbone chain length less than 50, we simulate 25 chains, for the PE100 simulation, we use 50 chains. The initial configurations for all the systems were generated using the method previously described by Mondello.[44] All chains are generated in all-*trans* configurations and placed in a cubic cell whose dimensions are large enough to ensure that there is no chain overlap. The MD simulation is run for a period of 200 ps while the size of the simulation box is gradually reduced to result in the desired density.

Calculated structural properties. We determine both structural and dynamic properties with the three force fields: OPLS, NERD, and TraPPE. Chain dimensions are quantified by the radius of gyration:

$$R_g = \left\langle \sqrt{\frac{\Sigma_i m_i (\mathbf{r}_i - \mathbf{r}_{\mathrm{CM}})^2}{M}} \right\rangle_N, \tag{4}$$

where $\mathbf{r}_i$ and m_i are the position and mass of each united atom and $\mathbf{r}_{\mathrm{CM}}$ and M are the position of the center of mass and mass of the chain containing atom i. The end-to-end distance is defined as the distance between the first and last atoms on the chain.

To quantify structure, we consider the radial distribution function,

$$g(r) = \frac{\langle \rho(r')\rho(r'+r)\rangle}{\langle \rho(r')\rangle^2}, \tag{5}$$

where $\rho(r')$ and $\rho(r'+r)$ are instantaneous densities of united atoms at the locations r' and $r'+r$ and angular brackets indicate averages over all r' positions in the simulation box.

Calculated dynamic properties. We make two comparisons to experimental data. In the first, the self-intermediate scattering function

$$S_{\mathrm{self}}(Q,t) = \frac{I^{\mathrm{inc}}(Q,t)}{I^{\mathrm{inc}}(Q,0)} = \frac{\langle \Sigma_{ij} c_i b_i^{\mathrm{inc}} \sin[Q\cdot r_i(t)]/[Q\cdot r_i(t)]\rangle}{\Sigma c_i b_i^{\mathrm{inc}}} \tag{6}$$

is compared with quasielastic neutron scattering (QENS) data from hydrogenated samples and other experimental probes of segmental dynamics. In Eq. (6), c_i is the atomic species concentration, b_i^{inc} is the incoherent scattering length, and $r_i(t) = r_i(t+t_0) - r_i(t_0)$. Due to the large incoherent scattering cross section of hydrogen measurements made on hydrogenated samples are dominated by incoherent scattering (>95% of total scattering) and reflect self motion. Thus Eq. (6) neglects the small contribution from coherent scattering. Unless stated otherwise, the decays $S(Q,t)$ and relaxation times discussed are for the self-intermediate scattering function defined in Eq. (6). In one case, we compare to QENS data collected on a neutron spin echo instrument with a partially deuterated sample. In the absence of hydrogen, scattering is mainly coherent and reflects collective motion:

$$S_{\mathrm{coll}}(Q,t) = \frac{I^{\mathrm{coh}}(Q,t)}{I^{\mathrm{coh}}(Q,0)} = \frac{\Sigma_{ij}\langle c_i c_j b_i^{\mathrm{coh}} b_j^{\mathrm{coh}} \sin[Q\cdot r_{ij}(t)]/[Q\cdot r_{ij}(t)]\rangle}{\Sigma_{ij}\langle c_i c_j b_i^{\mathrm{coh}} b_j^{\mathrm{coh}} \sin[Q\cdot r_{ij}(0)]/[Q\cdot r_{ij}(0)]\rangle}. \tag{7}$$

In the above, b_i^{coh} is the coherent scattering length and $r_{ij} = r_j(t+t_0) - r_i(t_0)$, where the indices i and j represent different scattering centers. The contribution of incoherent scattering

TABLE II. Summary of simulations.

Polymer M_W:g/mol	Temperature (K)	Density (g/ml)	R_g (±0.5 Å)	Box length (Å)	End-to-end vector ACF decay time (ns)
PE100 (M_W:1402)	504	0.7193	16.2	54.58	1.1
	423	0.7637	17.1	53.42	20.7
	390	0.7835	17.2	52.96	36.4
aPP40 (M_W:828)	523	0.6886	8.2	36.82	1.5
	510	0.6957	8.1	36.69	1.7
	490	0.7068	8.0	36.50	1.9
	475	0.7152	8.0	36.36	2.0
	423	0.7452	8.0	35.86	5.8
	400	0.7589	8.1	35.65	7.2
	384	0.7685	8.2	35.50	14.8
	364	0.7808	8.3	35.31	24.7
	344	0.7932	8.2	35.12	47.0
	322	0.8071	8.4	34.92	120.0
aPP54 (M_W:1122)	340	0.8029	9.7	41.14	95.0
iPP42 (M_W:870)	450	0.7307	8.2	36.70	8.9
hhPP42 (M_W:870)	423	0.7735	9.0	36.00	9.0
	400	0.7866	9.3	35.81	23.5
	381	0.7974	9.3	35.68	28.7
	366	0.8061	9.2	35.51	55.4
	344	0.8180	9.2	35.36	62.3
	322	0.8317	9.5	35.14	135.0
PEP42 (M_W:750)	423	0.7628	9.4	34.70	1.7
	400	0.7656	9.4	34.54	6.3
	384	0.7759	9.5	34.39	10.8
	364	0.7868	9.4	34.23	17.3
	336	0.8024	9.5	34.00	28.3
	317	0.8131	9.9	33.86	34.8
	294	0.8263	9.8	33.68	115.0

[~30%] is not negligible in this case and thus we include it in the comparison:

$$S(Q,t) = \frac{I^{\mathrm{coh}}(Q,t) + I^{\mathrm{inc}}(Q,t)}{I^{\mathrm{coh}}(Q,0) + I^{\mathrm{inc}}(Q,0)}. \quad (8)$$

For united atoms, scattering lengths are represented as a sum of the constituent scattering lengths, for example $b_{\mathrm{CH_2}} = b_{\mathrm{C}} + 2b_{\mathrm{H}}$.

III. EXPERIMENTAL DETAILS

A wide body of segmental dynamics measurements is available for the polyolefins. The segmental dynamics of aPP,[45–55] hhPP,[56–58] PEP,[57,58] and PE[41,59–64] have been measured by a variety of techniques. Here we add data for PEP and aPP measured using QENS. Such data have previously been reported,[47,57] although over different temperature ranges.

Materials preparation and characterization. aPP was purchased from American Polymer Standards Corporation. PEP was prepared by H_2 saturation of polyisoprene. The precursor polymer was synthesized in benzene with a *sec*-butyllithium initiator and a degassed methanol terminator using *in vacuo* anionic polymerization techniques.[65,66] Complete saturation of the double bonds was verified using ^{13}C NMR. The calorimetric glass transition temperatures were measured with a TA Instruments Q1000 differential scanning calorimeter (DSC) on 10–15 mg samples. The T_g values are reported as the midpoint of 10 K/min DSC scans. The molecular weight and polydispersity of PEP were determined by GPC using a Waters 2414 RI detector and are reported with respect to a universal polystyrene calibration curve.[67] The Mark–Houwink–Sakurada coefficients for PEP are $K = 4.22 \times 10^{-4}$ and $\alpha = 0.68$.[68] A summary of the characterization results from gel permeation chromatography and differential scanning calorimetry is given in Table III.

Neutron scattering measurements. QENS measurements were performed at the NIST Center for Neutron Research in Gaithersburg, MD, USA on two instruments: the disk-chopper time-of-flight spectrometer (DCS) (Ref. 69) and the NG2 high flux backscattering spectrometer (HFBS).[70] Table IV summarizes the temperatures at which dynamics were measured by QENS. The target values illustrate the temperatures at which measurements were made relative to the sample's T_g. In all cases samples were held for 1 h prior to measurement to allow thermal equilibration.

In both sets of measurements the samples were held in annular-shaped thin-walled aluminum cans and mounted on

TABLE III. Properties of measured samples.

Polymer	M_w (g/mol)	M_w/M_n	T_g (K)
aPP	830	1.12	208
PEP	6690	1.27	205

TABLE IV. Summary of QENS experiments.

	aPP		PEP	
Target	DCS	HFBS	DCS	HFBS
T_g+50	263	259	256	254
T_g+70	283	279	276	273
T_g+90			296	292
T_g+100	303	305		
T_g+110			316	318

closed cycle refrigeration units. To attain a neutron transmission rate of 90% and minimize the effects of multiple scattering, the samples were pressed to a thickness of 0.10 mm. The disk chopper spectrometer uses an incident monochromatic neutron beam of fixed wavelength and a detector array resolves the energy of the scattered neutrons based on their flight times. The DCS was operated with an incident wavelength of 4.2 Å (medium resolution) for measurements on PEP and 5.6 Å (low resolution) for aPP. Both conditions result in an energy resolution, full width at half maximum (FWHM), of 81.6 μeV and measurement window ranging from 0.2–51 ps. The high flux-backscattering spectrometer Doppler shifts neutrons about an incident wavelength of 6.27 Å to produce a range of incident energies. The detector arrays only measure neutrons scattered with a particular final energy: 2.08 meV. The instrument was operated at a dynamic range (energy transfer) of ± 17 μeV, resulting in a resolution (FWHM) of 0.80 μeV. These conditions result in an accessible time window of 243 to 5170 ps. Measurements on the DCS were made over a 6 h time period and those on the HFBS were made for 10 h. The resolutions of both instruments were measured using a vanadium sample at 295 K. The Data Analysis and Visualization Environment (DAVE) (Ref. 71) software developed at NIST, is used to correct for detector efficiency, and subtract the scattering from an empty aluminum can and the background. The data are binned into groups around average momentum transfer values of 0.63–2.71 Å^{-1}. The instrumental resolutions are removed when the dynamic structure factor, $S(Q,\omega)$ is Fourier-transformed into the time domain.[72] Both samples were hydrogenated and reflect self-motion.

IV. DATA TREATMENT

In this section, we describe the treatment of both the experimental and simulation data. We expect that measurements of aPP and PEP will reflect both rotation of the methyl side groups and segmental relaxation of the main chain. In the frequency domain these are convoluted processes: $S(Q,\omega)=S_{\mathrm{rot}}(Q,\omega)\otimes S_{\mathrm{seg}}(Q,\omega)$ and become a product, $S(Q,t)=S_{\mathrm{rot}}(Q,t)\cdot S_{\mathrm{seg}}(Q,t)$, when Fourier-transformed to the time domain. To remove the rotational contribution, we use previously reported measurements that isolate methyl group rotation.[45,57] The parameters describing rotation were reported in the frequency domain. To use them in the time domain, we construct a model function based on the reported fit parameters and Fourier transform it to the time domain.

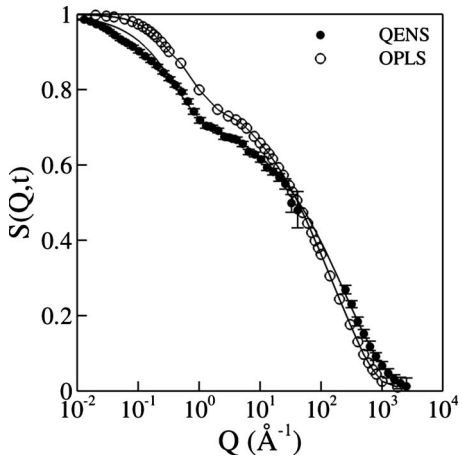

FIG. 5. Representative fits to experimental and simulation data. (a) QENS data with methyl group rotations removed for PEP at 296 K and Q =0.99 Å^{-1}. (b) Simulation data for PEP at 294 K and Q=0.99 Å^{-1}. Differences at short times arise from the different caging behavior of hydrogen atoms (QENS) and the united atoms of the simulation.

This is used to remove the rotational contribution, for comparison to simulation data which does not contain methyl group rotations.

Whether calculated from simulation or obtained from QENS data as described above, the segmental process has two parts, $S(Q,t)_{\mathrm{seg}}=S(Q,t)_{\mathrm{fast}}\cdot S(Q,t)_{\mathrm{slow}}$, as illustrated in Fig. 5. The fast process reflects movement within a local cage; this motion is fit with an exponential decay and will not be considered further. The slow process is the target of our investigation: we fit this with a stretched exponential.[73] In the resulting expression for $S(Q,t)_{\mathrm{seg}}$,

$$S(Q,t)_{\mathrm{seg}}=\left\{\mathrm{EISF}_{\mathrm{fast}}+(1-\mathrm{EISF}_{\mathrm{fast}})\times\exp\left[-\left(\frac{t}{\tau_{\mathrm{fast}}}\right)\right]\right\}\exp\left[-\left(\frac{t}{\tau_{\mathrm{slow}}}\right)^{\beta}\right]. \quad (9)$$

The appearance of an elastic incoherent structure factor (EISF) partitions the decay between the two processes. Representative fits for both experiment and simulation are provided in Fig. 5. To account for the interdependence of the fit parameters, we assign error bars to τ_{slow} and β. These error bars represent the range of values each may take, regardless of the values of other parameters.[72] Thus, values of τ_{slow} or β outside of the error bars given in Figs. 9–11 cannot describe the data.

V. RESULTS AND DISCUSSION

The remainder of the paper focuses on the segmental motion (slow process) of hhPP, PEP, PE, and aPP. We compare experimental results with those obtained using the three force fields, which not only reveals the force field numerically closest to the experimental data, but also the dynamic response to changes in intermolecular and torsional potentials. While our main focus is on dynamics, we first consider structural properties.

Structural properties. In this section, we consider the representative structural properties as assessed by the radial

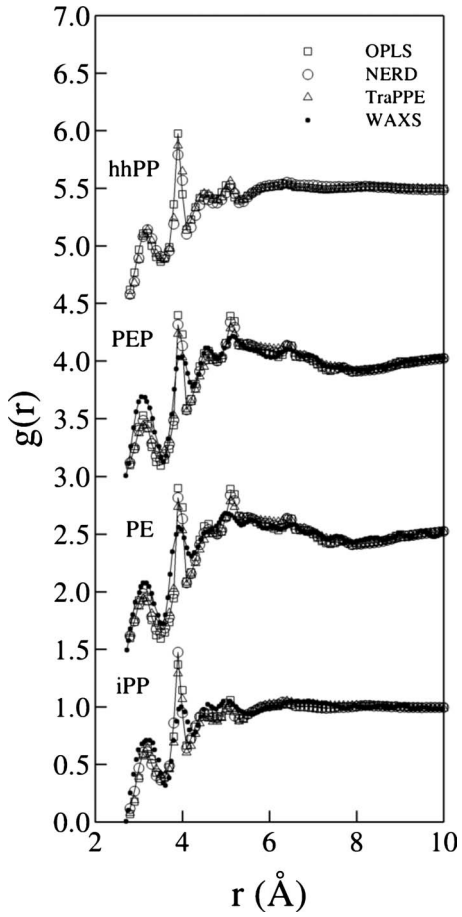

FIG. 6. Comparison of radial distribution functions, $g(r)$ from WAXS (Ref. 74) and simulation. hhPP, PE, and PEP are offset on the y-axis for clarity.

distribution function $[g(r)]$ and chain dimensions. We compare wide angle x-ray diffraction (WAXS) measurements, Fourier transformed to provide $g(r)$ on PE (423 K), iPP (453 K), and PEP (298 K) (Ref. 74) to the same quantity calculated directly from simulation. Because the intensity of WAXS measurements depends on electron density and is thus not sensitive to hydrogen atom correlations, a direct comparison between experimental measurements and UA simulation results is possible. Although experimental data are not available, we include simulation results for hhPP; this material would be most influenced if changes in the torsional barrier heights are important. As illustrated in Fig. 6, the three force fields represent $g(r)$ equally well for both linear (PE) and branched materials. This implies that the variations in the strength of the intermolecular interactions and the height of the torsional barriers in the branched materials do not have significant impact on the structural properties of the materials. With respect to the torsional barriers, although the transition rates may differ, the partitioning between *trans*- and *gauche* configurations does not.

As a second measure of structure, we compare chain dimensions as quantified by the radius of gyration and the chain end-to-end distance. In Fig. 7, we present the chain dimensions for each material. Like $g(r)$, no significant difference appears, indicating that neither the torsional barriers nor the strength of the intermolecular interactions have a large impact on chain dimensions.

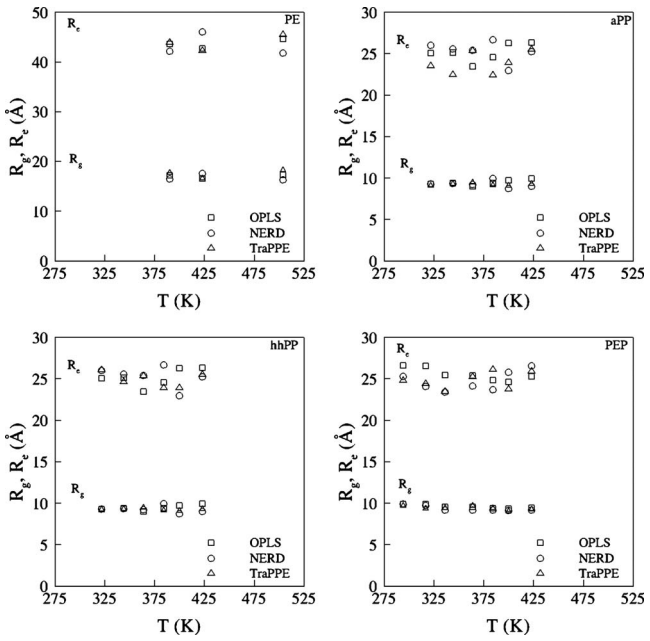

FIG. 7. (a)–(d) compare the chain dimensions (R_g and R_e) of PE, aPP, hhPP, and PEP as calculated from simulation.

Dynamic properties. In this section, we discuss segmental dynamics and its connection to the variations in intermolecular and torsional potentials. To establish the general validity of all force fields, we compare with available experimental data including QENS. Two challenges arise with this comparison: the temperature ranges of the data sets do not overlap, and the molecular weights of the simulated and experimental samples differ, which influences dynamics via the molecular weight dependence of T_g. In two cases, experimental data are available at the same temperature and molecular weight: as the simulation PE100 at 504 K,[64] and aPP54 at 340 K.[45] For these two cases, we directly compare decay of the experimental and simulated scattering functions. We present the two direct comparisons in Fig. 8. We do not need to remove methyl group rotation from the experimental data because it is absent in these measurements: PE100 does not have methyl groups and the measurements on deuterated aPP54 reflect coherent scattering, which is not sensitive to methyl group rotation. The comparison for PE100, presented in Fig. 8(a), supports two conclusions: that all three force fields provide similar results, and that they closely follow the experimental data. The results in Fig. 8(a) are for $Q = 0.8$ Å^{-1}. The results are similar for other spatial scales. The first conclusion extends to lower temperatures, as indicated by the data at 423 and 390 K, also provided in the figure. In contrast, the comparison for aPP54, presented in Fig. 8(b), displays both a larger variation among force fields, and larger difference from the experimental data. This result is not surprising; as discussed above, the force fields vary in their description of branched materials. We will also see below that differences become more pronounced with decreasing temperature.

For the remainder of the comparisons, we collect all available experimental data in material specific plots, remove the influence of molecular weight, and fit to a Vogel form.

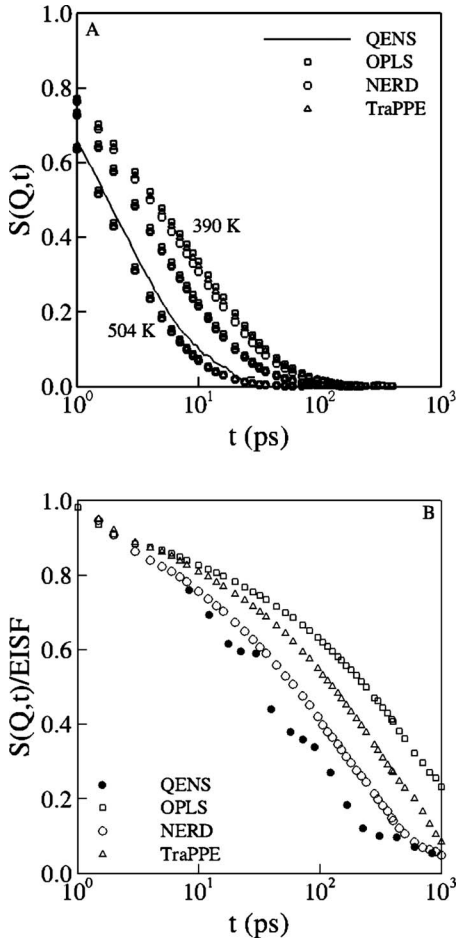

FIG. 8. Direct comparison of scattering functions from QENS and simulation. (a) Incoherent scattering from hydrogenated PE [MW: 1402 g/mol] at 504 K and $Q=0.8$ Å^{-1}. Experimental data from Ref. 64. Simulation data shown at 504, 423, and 390 K. (b) Coherent scattering from deuterated aPP [MW: 1270 g/mol] and simulated aPP54 [MW: 1122 g/mol] at $Q=1.1$ Å^{-1} and 340 K. Experimental data from Ref. 45. The fast process has been removed from both sets of data.

We then use the Vogel fits to represent the collection of experimental data when compared with simulation results. Segmental relaxation times are obtained, as discussed above. The characteristic relaxation time,

$$\tau_c = \frac{\tau_{\text{slow}}}{\beta_{\text{slow}}}\Gamma\left(\frac{1}{\beta_{\text{slow}}}\right), \tag{10}$$

folds together τ_{slow} and β_{slow} and is often used in comparing different data sets. To represent the collective body of experimental data, we collect the data in a Vogel plot for each material. Differences in T_g due to molecular weight are accounted for by presenting the characteristic relaxation times as a function of T/T_g, where T_g is the glass transition temperature at the molecular weight for each experiment. Figure 9 presents characteristic times for the segmental relaxation of aPP, PEP, hhPP, and PE. Because QENS has spatial resolution, whereas the other techniques do not, we need to choose one spatial scale at which to do the comparison. We choose $Q=0.99$ Å^{-1} (for aPP and PEP) and $Q=0.63$ Å^{-1} (for hhPP) for this purpose, because these are the spatial scales which most accurately reflect NMR and dielectric experiments. The influence of molecular weight via T_g is seen

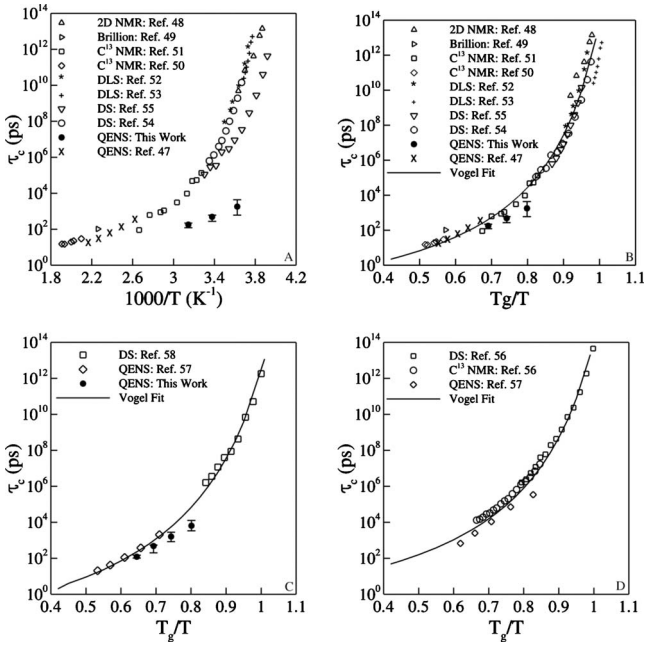

FIG. 9. Summary of experimental data for aPP, PEP, and hhPP. (a) Dynamic measurements of aPP in $1000/T$ representation. (b) The data in part (a) scaled by respective T_g of each sample. (c) PEP. (d) hhPP. QENS spatial scales which most accurately reflect other measurements are $Q=0.99$ Å^{-1} for aPP and PEP, and $Q=0.63$ Å^{-1} for hhPP.

by comparing Fig. 9(a) and Fig. 9(b), where the data are plotted versus $1000/T$ and T_g/T for aPP. To obtain Vogel lines representing the collection of experimental data, we use

$$\tau_{\text{seg}}(T) = \tau_\infty \exp\left[\frac{B'}{T/T_g - T_0'}\right], \tag{11}$$

where B' and T_0' are scaled parameters, related to the Vogel B and T_0 parameters through the following relationships: $B=B'T_g$ and $T_0=T_0'T_g$. Table V summarizes the universal fit parameters: τ_∞, B', and T_0' for all of the materials. Our QENS measurements on aPP and PEP are consistent with other available data.

In Fig. 10 we compare simulation data with the collective Vogel lines. As expected, the segmental dynamics of PE are invariant to force field. As branch points are added without the CH–CH bond (the series PE, PEP, aPP in Fig. 10) differences between force fields emerge, in particular for low temperatures. As anticipated above, the OPLS force field is the slowest of the three, with this effect more pronounced as the number of branch points increases. The TraPPE force field is slower than NERD, which suggests that the softer nonbonded CH interactions do not lead to faster dynamics. When the CH–CH bond is added (hhPP), differences between materials are reduced significantly compared to aPP,

TABLE V. Vogel fit parameters.

Material	MW (g/mol)	τ_∞ (ps)	B'	T_o'
aPP	830	0.30	3.774	0.889
hhPP	870	1.20	5.73	0.823
PEP	750	0.11	6.111	0.811

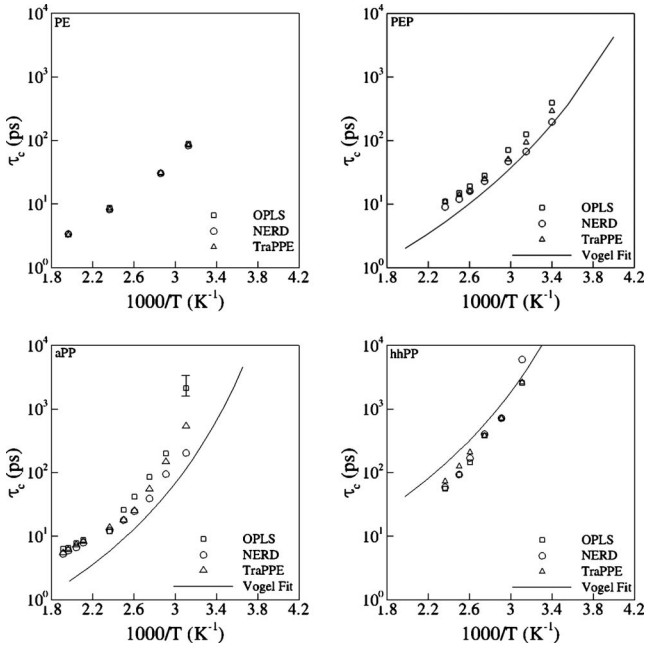

FIG. 10. Comparison of simulation data to the Vogel lines representing all available experimental data. Each part illustrates one material as labeled in the figures. Error bars within the size of the data point are omitted for clarity. Spatial scales are $Q=0.99$ Å^{-1} for aPP and PEP, and $Q=0.63$ Å^{-1} for hhPP.

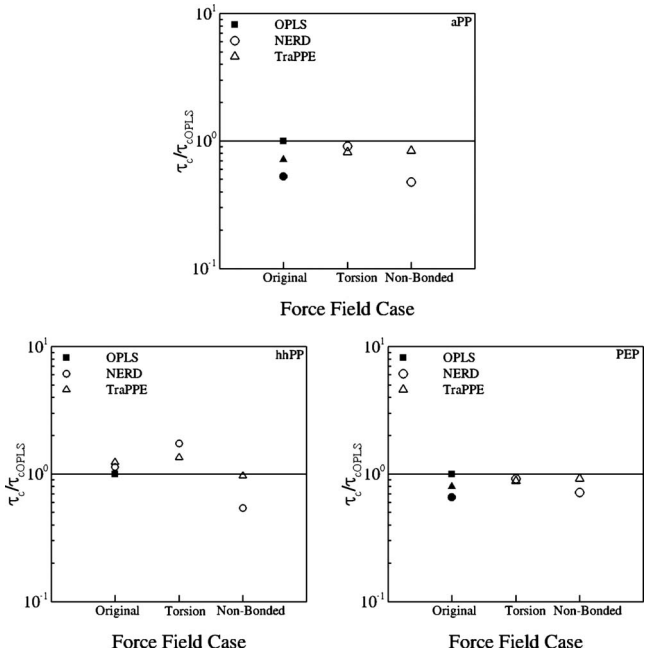

FIG. 12. Comparison of parameter effects on dynamic properties in materials which show a force field dependence: aPP, hhPP, and PEP. All values are normalized by the average relaxation time in OPLS simulations. A dashed line at a reduced relaxation time of 1.0 has been added as a guide to the eyes. Reduced relaxation times of original force fields appear as filled symbols.

which has the same number of branch points. Agreement between characteristic relaxation times from simulation and the fit line characterizing the available experimental results is adequate, and we expect similar trends different spatial scales, where QENS data cannot be compared directly with other techniques. In cases where differences in force fields emerge at low temperature, the NERD force field provides the best correlation with experimental data. Values of the stretching parameter are similar for all force fields: those from NERD are compared with those from experimental QENS data in Fig. 11.

For the branched materials aPP and PEP, the three force fields describe dynamics differently while maintaining similar descriptions of static properties. We now consider the origin of these differences and the relation of various parts of

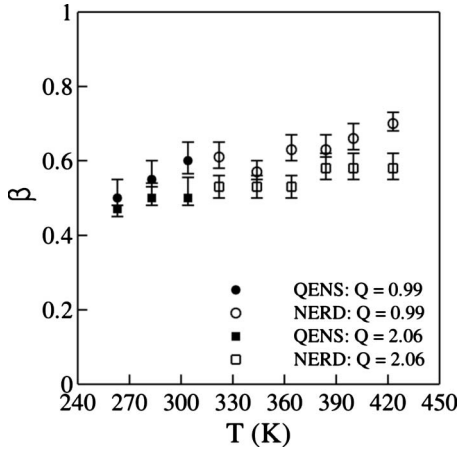

FIG. 11. Comparison of the stretching parameters for aPP from experiment and simulation with the NERD force field. Other materials and force fields produce similar figures.

the force field to dynamics in general. The OPLS force field results in the slowest dynamics. This force field has both the highest barrier for rotation about the CH_2-CH bond and the largest well depths for nonbonded interactions. Either will slow dynamics and thus we begin by assessing the relative influence of the two. To consider this, we create four "hybrid" force fields. Each hybrid begins with the OPLS force field and swaps either the torsional or nonbonded potentials with one of the remaining two force fields. Thus the NERD-torsion hybrid combines the OPLS nonbonded potentials with the NERD torsion potentials. This has the effect of lowering barriers to torsional transitions while keeping nonbonded interactions the same. Using the four hybrid force fields, we ran simulations of aPP, hhPP, and PEP at 364 K, and obtained characteristic times for the self-intermediate scattering functions at $Q=0.99$ Å^{-1}. The results are compared with the original force fields in Fig. 12. Plotted on the y-axis is the ratio of the characteristic times to that of the OPLS force field. In the first column, marked "original," the ratios NERD/OPLS and TraPPE/OPLS signify the dynamic differences between force fields. The second column, labeled "torsion," denotes the results of changing OPLS torsional potentials to those from the other two force fields, both of which reduce torsional barriers. The extent to which this explains differences between force fields may be determined by comparing the values of the original and torsion data points: the closer the two values, the more changing torsional barriers contribute to differences in dynamics between force fields. The third column repeats this procedure for nonbonded interactions. Both torsional hybrids reduce the characteristic times compared to OPLS, as expected based on lowered torsional barriers. The nonbonded hybrids also re-

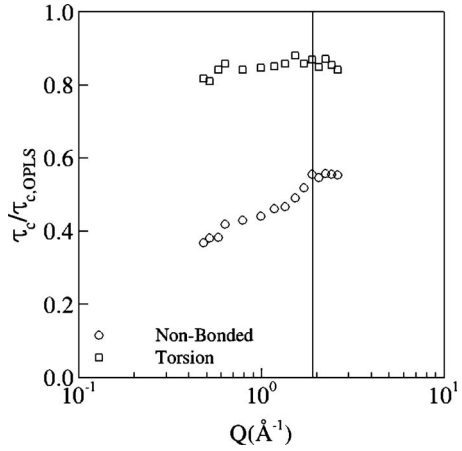

FIG. 13. Comparison of the spatial dependence different potentials have on dynamics. Hybrid force fields are created by inserting the appropriate NERD parameters into the OPLS force field.

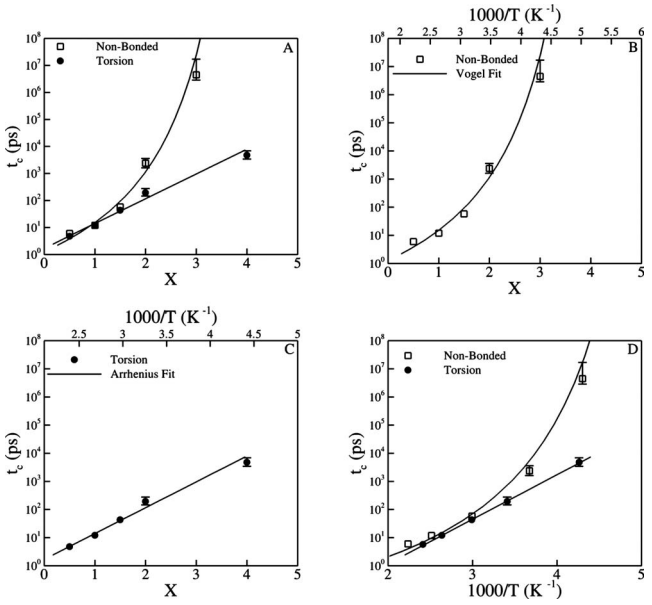

FIG. 14. (a) Relaxation times with altered torsion barriers and nonbonded interaction strength. (b) Temperature "map" to altered nonbonded interaction strengths. (c) Temperature map to altered torsion barriers. (d) Relaxation temperature map of dynamics. Hybrid force fields are created by multiplying the appropriate OPLS interaction parameters by the factor *X*.

duce characteristic times. In the case of NERD, this is the dominant influence: the nonbonded hybrid is almost the same as changing both nonbonded and torsional interactions. The situation for TraPPE is more balanced: individual nonbonded potentials change in different ways, with the overall effect less pronounced. Using the NERD hybrids, we now ask if the spatial scale of the measurement influences the relative contributions of torsional barriers and nonbonded interactions. In Fig. 13, we plot the ratio of hybrid to OPLS characteristic times as a function of spatial scale. When lowering only torsional barriers, the result is independent of spatial scale, whereas the effect of reducing nonbonded interaction strength increases with the spatial scale of the measurement. At spatial scales smaller than ~3 Å, the effect levels off. This behavior is consistent with the idea that the effect of nonbonded interactions is cumulative. Within 3 Å, nonbonded interactions are intramolecular, and arise primarily from one to five interactions. These interactions influence dynamics in a way similar to the torsional barriers. As the spatial scale increases, intermolecular nonbonded interactions become prevalent. A given united atom moves through a series of local "cages" formed by intermolecular contacts. If the attractive strength of these cages is reduced, escape from the cage is faster. Roughly, the spatial scale of the measurement corresponds to the distance at which self-correlation is lost: if a given atom has moved this distance during the time interval probed, its self-intermediate scattering function is zero. As the spatial scale increases, cage events are first introduced, and then repeated. As is apparent from Fig. 13, each such event serves to slow dynamics: as the spatial scale varies from 3 to 15 Å, dynamics slowed by 33%.

The influence of lowering torsional barriers has previously been addressed[75,76] and led to an interpretation of the β-relaxation with sampling of all torsional angles. The α-relaxation was then associated with this sampling reaching its equilibrium probability due to significant motion of the surrounding polymer matrix. This interpretation, together with our discussion above, suggests an association of torsional barriers with the β-relaxation, and nonbonded interaction strength with the α-relaxation. If this is true, then one would expect that increasing torsional barriers would have the same influence as lowering temperature has on β-relaxation times, whereas increasing the strength of nonbonded interactions would have the same effect as lowering temperature has on α-relaxation times. In Fig. 14, we test this idea by raising torsional barriers and nonbonded interaction strength independently by a factor X. When barrier heights and nonbonded interactions are near their nominal values, relaxation times change in a similar way no matter which interaction is altered. This is similar to high temperature behavior where the α- and β-relaxations are observed as a single merged process. As X increases, raising torsional barriers and increasing nonbonded interaction strength have very different effects. Higher torsional barriers cause characteristic times to increase linearly with X, much as β-relaxation times increase linearly as temperature is decreased. Stronger nonbonded attractions cause a nonlinear increase in characteristic times, much like the behavior of the α-relaxation at low temperature. The value of X should be related to temperature, with the connection for torsional barriers and nonbonded interactions not necessarily equivalent as Fig. 14(a) suggests. We test this by mapping X torsion to the temperature dependence of the β-relaxation,[55] and X nonbonded to the Vogel line describing available experimental data. Each mapping is provided in the Fig. 14: part (b) shows the mapping of nonbonded interaction strength to the Vogel line representing the segmental or α-relaxation of aPP, and part (c) the mapping of torsional barriers to the Arrhenius line describing the β-relaxation. Comparing these figures, the correspondence of X with temperature is slightly different for the two cases. In part (d) of the figure, we plot the relaxation times from each series versus their mapped tem-

peratures. The result is similar to relaxation "maps" showing the divergence of α- and β-relaxations at low temperature.

These results show a strong association between the α-relaxation and the nonbonded interaction strength. They also confirm previous suggestions that torsional barrier strength is related to the β-relaxation.[75,76] Work in our group[77–79] and others[80–82] has shown that the softer nonbonded potentials characteristic of coarse-grained models lead to acceleration of dynamics. We also linked the extent of the acceleration to the monomeric friction factor, again suggesting association between nonbonded interaction strength and the α-relaxation. It appears that the point at which the α- and β-relaxation bifurcates is related to the relative strengths of nonbonded interaction energies and torsional barriers. A similar point was made for polybutadiene, not by raising the torsional barriers, but by removing them entirely.[36] In the resulting freely rotating PBD, the α-process is unchanged while the β-process is much faster.

VI. CONCLUSIONS

We tested three force fields for their ability to describe dynamics of polyolefins. More important than the results of this test are the relative implications of different interactions on the resulting dynamics. We find that decreased torsional barriers lead to faster dynamics, with the influence independent of spatial scale. In contrast, decreasing nonbonded interactions lead to faster dynamics, but the effect is larger and dependent on spatial scale. This led us to consider the effects of increasing both torsional barriers and nonbonded interactions. The increase had the expected effect of slowing dynamics, but the way in which dynamics were slowed varied considerably. Increasing the difficulty of nearest neighbor cage escapes and torsional barrier crossings more difficult both act like lowering the temperature: the first induces a slowdown with the Vogel dependence of the α-relaxation, while the second induces a slow down with the Arrhenius dependence of the β-relaxation.

ACKNOWLEDGMENTS

Financial support for this work was provided by the National Science Foundation via the Polymers Program, through a CAREER Grant No. DMR-0134910 and the Energy for Sustainability Program No. CBET 0730502.

[1] H. W. Spiess, Annu. Rev. Mater. Sci. **21**, 131 (1991).
[2] R. Kimmich and N. Fatkullin, Adv. Polym. Sci. **170**, 1 (2004).
[3] P. A. Mirau, *A Practical Guide to Understanding the NMR of Polymers* (Wiley, Hoboken, 2005).
[4] F. Kremer, J. Non-Cryst. Solids **305**, 1 (2002).
[5] J. P. Runt and J. J. Fitzgerald, *Dielectric Spectroscopy of Polymeric Materials: Fundamentals and Applications* (American Chemical Society, Washington, D.C., 1997).
[6] F. Kremer and A. Schönhals, *Broadband Dielectric Spectroscopy* (Springer, Berlin, 2003).
[7] J. Higgins and H. Benoît, *Polymers and Neutron Scattering* (Clarendon, Oxford, 1996).
[8] M. Bée, *Quasielastic Neutron Scattering* (Adam Higler, Bristol, 1988).
[9] D. Richter, Physica B **276**, 22 (2000).
[10] R. Pecora, *Dynamic Light Scattering: Applications of Photon Correlation Spectroscopy* (Plenum, New York, 1985).
[11] W. Burchard, Adv. Polym. Sci. **48**, 1 (1983).
[12] J. Meissner, Annu. Rev. Fluid Mech. **17**, 45 (1985).
[13] J. D. Ferry, *Viscoelastic Properties of Polymers* (Wiley, New York, 1980).
[14] E. Jaramillo, D. T. Wu, G. S. Grest, and J. G. Curro, J. Chem. Phys. **120**, 8883 (2004).
[15] D. Heine, D. T. Wu, J. G. Curro, and G. S. Grest, J. Chem. Phys. **118**, 914 (2003).
[16] J. D. Londono, J. K. Maranas, M. Mondello, A. Habenschuss, G. S. Grest, P. G. Debenedetti, W. W. Graessley, and S. K. Kumar, J. Polym. Sci., Part B: Polym. Phys. **36**, 3001 (1998).
[17] A. Neelakantan and J. K. Maranas, J. Chem. Phys. **120**, 465 (2004).
[18] A. Neelakantan and J. K. Maranas, J. Chem. Phys. **120**, 1617 (2004).
[19] J. K. Maranas, M. Mondello, G. S. Grest, S. K. Kumar, P. G. Debenedetti, and W. W. Graessley, Macromolecules **31**, 6991 (1998).
[20] J. K. Maranas, S. K. Kumar, P. G. Debenedetti, W. W. Graessley, M. Mondello, and G. S. Grest, Macromolecules **31**, 6998 (1998).
[21] P. V. K. Pant and R. H. Boyd, Macromolecules **25**, 494 (1992).
[22] P. V. K. Pant and R. H. Boyd, Macromolecules **26**, 679 (1993).
[23] G. D. Smith and D. Y. Yoon, J. Chem. Phys. **100**, 649 (1994).
[24] M. Mondello and G. S. Grest, J. Chem. Phys. **103**, 7156 (1995).
[25] T. J. McKnight, T. J. H. Vlugt, D. Ramjugernath, M. Starzak, P. Ahlström, and K. Bolton, Fluid Phase Equilib. **232**, 136 (2005).
[26] J. López-Lemus, M. Romero-Bastida, T. A. Darden, and J. Alejandre, Mol. Phys. **104**, 2413 (2006).
[27] W. L. Jorgensen, J. D. Madura, and C. Swenson, J. Am. Chem. Soc. **106**, 6638 (1984).
[28] M. G. Martin and J. I. Siepmann, J. Phys. Chem. B **102**, 2569 (1998).
[29] M. G. Martin and J. I. Siepmann, J. Phys. Chem. B **103**, 4508 (1999).
[30] S. K. Nath, F. A. Escobedo, and J. J. de Pablo, J. Chem. Phys. **108**, 9905 (1998).
[31] S. K. Nath and J. J. de Pablo, Mol. Phys. **98**, 231 (2000).
[32] S. K. Nath and R. Khare, J. Chem. Phys. **115**, 10837 (2001).
[33] J. I. Siepmann, S. Karaborni, and B. Smit, Nature **365**, 330 (1993).
[34] V. A. Harmandaris, V. G. Mavrantzas, D. N. Theodorou, M. Kröger, J. Ramírez, H. C. Öttinger, and D. Vlassopoulos, Macromolecules **36**, 1376 (2003).
[35] H. C. Andersen, J. Comput. Phys. **52**, 24 (1983).
[36] D. Bedrov and G. D. Smith, Macromolecules **38**, 10314 (2005).
[37] D. Bedrov and G. D. Smith, Macromolecules **39**, 8526 (2006).
[38] P. K. Depa and J. K. Maranas, J. Chem. Phys. **126**, 054903 (2007).
[39] W. Swope, H. Andersen, P. H. Berens, and K. R. Wilson, J. Chem. Phys. **76**, 637 (1982).
[40] H. J. C. Berendsen, J. P. M. Postma, W. F. van Gunsteren, A. DiNola, and J. R. Haak, J. Chem. Phys. **81**, 3684 (1984).
[41] D. S. Pearson, G. V. Strate, E. Vonmeerwall, and F. C. Schilling, Macromolecules **20**, 1133 (1987).
[42] A. K. Doolittle, J. Chem. Eng. Data **9**, 275 (1964).
[43] R. Krishnamoorti, Ph.D. dissertation, Princeton University, 1994.
[44] M. Mondello, H. J. Yang, H. Furuya, and R. J. Roe, Macromolecules **27**, 3566 (1994).
[45] V. Arrighi, R. Ferguson, R. E. Lechner, M. Telling, and A. Triolo, Physica B **301**, 35 (2001).
[46] V. Arrighi, C. Pappas, A. Triolo, and S. Pouget, Physica B **301**, 157 (2001).
[47] O. Ahumada, D. N. Theodorou, A. Triolo, V. Arrighi, C. Karatasos, and J. P. Ryckaert, Macromolecules **35**, 7110 (2002).
[48] D. Schaefer, H. W. Spiess, U. W. Suter, and W. W. Fleming, Macromolecules **23**, 3431 (1990).
[49] G. D. Patterson, J. Polym. Sci., Part B: Polym. Phys. **15**, 455 (1977).
[50] N. E. Moe, X. H. Qiu, and M. D. Ediger, Macromolecules **33**, 2145 (2000).
[51] A. Dekmezian, D. E. Axelson, J. J. Dechter, B. Borah, and L. Mandelkern, J. Polym. Sci., Part B: Polym. Phys. **23**, 367 (1985).
[52] G. Fytas and K. L. Ngai, Macromolecules **21**, 804 (1988).
[53] P. G. Santangelo, K. L. Ngai, and C. M. Roland, Macromolecules **29**, 3651 (1996).
[54] C. M. Roland, K. L. Ngai, P. G. Santangelo, X. H. Qiu, M. D. Ediger, and D. J. Plazek, Macromolecules **34**, 6159 (2001).
[55] K. Kessairi, S. Napolitano, S. Capaccioli, P. Rolla, and M. Wübbenhorst, Macromolecules **40**, 1786 (2007).
[56] E. Krygier, G. X. Lin, J. Mendes, G. Mukandela, D. Azar, A. A. Jones, J. A. Pathak, R. H. Colby, S. K. Kumar, G. Floudas, R. Krishnamoorti, and R. Faust, Macromolecules **38**, 7721 (2005).
[57] R. Pérez Aparicio, A. Arbe, J. Colmenero, B. Frick, L. Willner, D. Richter, and L. J. Fetters, Macromolecules **39**, 1060 (2006).
[58] J. A. Pathak, Ph.D. dissertation, The Pennsylvania State University,

(2000).
[59] X. H. Qiu and M. D. Ediger, Macromolecules **33**, 490 (2000).
[60] D. S. Pearson, L. J. Fetters, W. W. Graessley, G. V. Strate, and E. von Meerwall, Macromolecules **27**, 711 (1994).
[61] Y. P. Khanna, E. A. Turi, T. J. Taylor, V. V. Vickroy, and R. F. Abbott, Macromolecules **18**, 1302 (1985).
[62] G. B. McKenna, K. L. Ngai, and D. J. Plazek, Polymer **26**, 1651 (1985).
[63] D. Richter, L. Willner, and A. Zirkel, Macromolecules **27**, 7437 (1994).
[64] G. D. Smith, W. Paul, D. Y. Yoon, A. Zirkel, J. Hendricks, D. Richter, and H. Schober, J. Chem. Phys. **107**, 4751 (1997).
[65] M. Morton and L. Fetters, Rubber Chem. Technol. **48**, 359 (1975).
[66] D. Uhrig and J. W. Mays J. Polym. Sci., Part A: Polym. Chem. **43**, 6179 (2005).
[67] P. C. Painter and M. M. Coleman, *Fundamentals of Polymer Science: An Introductory Text* (Technomic, Lancaster, 1997).
[68] J. Mays, N. Hadjichristidis, and L. J. Fetters, Macromolecules **17**, 2723 (1984).
[69] J. R. D. Copley and J. C. Cook, Chem. Phys. **292**, 477 (2003).
[70] A. Meyer, R. M. Dimeo, P. M. Gehring, and D. A. Neumann, Rev. Sci. Instrum. **74**, 2759 (2003).
[71] The IDL-based program can be found at http://www.ncnr.nist.gov/dave.
[72] V. G. Sakai, C. Chen, J. K. Maranas, and Z. Chowdhuri, Macromolecules **37**, 9975 (2004).
[73] G. Williams and D. C. Watts, Trans. Faraday Soc. **66**, 80 (1970).
[74] J. D. Londono, A. Habenschuss, J. G. Curro, and J. J. Rajasekaran, J. Polym. Sci., Part B: Polym. Phys. **34**, 3055 (1996).
[75] D. Bedrov and G. D. Smith, Phys. Rev. E **71**, 050801 (2005).
[76] G. D. Smith and D. Bedrov, J. Non-Cryst. Solids **352**, 4690 (2006).
[77] P. K. Depa and J. K. Maranas, J. Chem. Phys. **123**, 094901 (2005).
[78] C. Chen, P. Depa, V. García-Sakai, J. W. Lynn, I. Peral, and J. R. D. Copley, J. Chem. Phys. **124**, 234901 (2006).
[79] C. Chen, P. Depa, J. K. Maranas, and V. García-Sakai, J. Chem. Phys. **128**, 124906 (2008).
[80] S. O. Nielsen, C. F. Lopez, G. Srinivas, and M. L. Klein, J. Phys.: Condens. Matter **16**, R481 (2004).
[81] L. Whitehead, C. M. Edge, and J. W. Essex, J. Comput. Chem. **22**, 1622 (2001).
[82] C. F. Lopez, S. O. Nielsen, P. B. Moore, J. C. Shelley, and M. L. Klein, J. Phys.: Condens. Matter **14**, 9431 (2002).